Emiliano Quinones Yumbla
School for Engineering of Matter,
Transport and Energy;
Ira A. Fulton Schools of Engineering,
Arizona State University,
Tempe, AZ 85281
e-mail: ejquino1@asu.edu

Dongting Li
School of Manufacturing Systems and Networks;
Ira A. Fulton Schools of Engineering,
Arizona State University,
Mesa, AZ 85212
e-mail: dongting@asu.edu

Tolemy M. Nibi
School for Engineering of Matter,
Transport and Energy;
Ira A. Fulton Schools of Engineering,
Arizona State University,
Tempe, AZ 85281
e-mail: tnibi@asu.edu

Daniel M. Aukes
School of Manufacturing Systems and Networks;
Ira A. Fulton Schools of Engineering,
Arizona State University,
Mesa, AZ 85212
e-mails: danaukes@asu.edu;
asme@idealabasu.com

Wenlong Zhang[1]
School of Manufacturing Systems and Networks;
Ira A. Fulton Schools of Engineering,
Arizona State University,
Mesa, AZ 85212
e-mails: wenlong.zhang@asu.edu

A Kinematically Constrained Kalman Filter for Sensor Fusion in a Wearable Origami Robot

Sensing for wearable robots is an ongoing challenge, especially given the recent trend of soft and compliant robots. Recently, a wearable origami exoshell has been designed to sense the user's torso motion and provide mobility assistance. The materials of the exoshell contribute to a lightweight design with compliant joints, which are ideal characteristics for a wearable device. Common sensors are not ideal for the exoshell as they compromise these design characteristics. Rotary encoders are often rigid metal devices that add considerable weight and compromise the flexibility of the joints. Inertial measurement unit sensors are affected by environments with variable electromagnetic fields and therefore not ideal for wearable applications. Hall effect sensors and gyroscopes are utilized as alternative compatible sensors, which introduce their own set of challenges: noisy measurements and drift due to sensor bias. To mitigate this, we designed the Kinematically Constrained Kalman filter for sensor fusion of gyroscopes and Hall effect sensors, with the goal of estimating the human's torso and robot joint angles. We augmented the states to consider bias related to the torso angle in order to compensate for drift. The forward kinematics of the robot is incorporated into the Kalman filter as state constraints to address the unobservability of the torso angle and its related bias. The proposed algorithm improved the estimation performance of the torso angle and its bias, compared to the individual sensors and the standard Kalman filter, as demonstrated through bench tests and experiments with a human user. [DOI: 10.1115/1.4056986]

Keywords: Estimation, Kalman filtering, medical robotics, robotics, sensor fusion, sensors and sensor networks, service/rehabilitation robots

1 Introduction

Recently, a new trend for wearable devices referred to as wearable origami exoshell has been designed, which consists of origami modular structures that combine rigid and flexible materials [1]. The exoshell is fabricated with layers of cardboard and flexible polyester film, contributing to a lightweight and compliant device, which are ideal characteristics for a wearable design. The origami exoshell robot consists of triangular origami links that together form a serial link robot with flexible joints. This device was designed to be worn on the back of a human, as shown in Fig. 1, to sense the user's torso motion and provide mobility assistance.

Sensing for wearable robots is an ongoing challenge, especially given the recent trend of soft and compliant robots [2]. While placing rotary encoders at the robot's joints has been a common solution [3], our origami exoshell design is not ideal for traditional encoders. Rotary encoders are often rigid metal devices that add considerable weight to the design. Furthermore, the rigidness of typical encoders affects the robot's structural compliance, compromising the flexibility of the layer and therefore the mobility of the joint [4].

As an alternative, inertial measurement units (IMU) are used to measure the robot and human kinematics [5]. IMUs consist of a gyroscope, an accelerometer, and a magnetometer. Although some studies have achieved good performance with IMU sensors, they often rely on using the magnetometer for drift correction [6]. This method is not ideal for long-term wearable applications as it has been commonly reported that changes in the environment's magnetic field affect the magnetometer's reliability [7]. Furthermore, it is often required to embed electronic hardware within the robot, which will inflict even more disturbances due to the magnetic field generated by these electronic components.

To overcome limitations in individual sensors, many studies have utilized sensor fusion algorithms, such as the Kalman filter (KF). Several studies have been successful at improving estimation performance with the KF using a serial link robot similar to our origami exoshell. For example, in several studies [8,9], a KF was designed to fuse multiple sensors in a rigid and fixed serial link robot. While performance was improved, the algorithms have the underlying assumption that the base coordinate frame is fixed and therefore cannot be applied when the robot is in free motion while worn by a human user. Some studies have in fact focused on KF for wearable applications [10,11], but they are commonly designed for estimating the human alone and do not take into account integration with a wearable robot system which introduces electromechanical disturbances to the sensors. In Ref. [10], the authors fuse the information from multiple IMU, but they do not take into account magnetic disturbances from either the environment or a wearable robot system.

The sensor hardware limitations discussed are hard constraints of our origami robot due to its design characteristics. Since placing an encoder is not possible and using magnetometers is not ideal, in this

[1]Corresponding author.
Manuscript received October 7, 2022; final manuscript received February 12, 2023; published online March 16, 2023. Assoc. Editor: Alexander Leonessa.

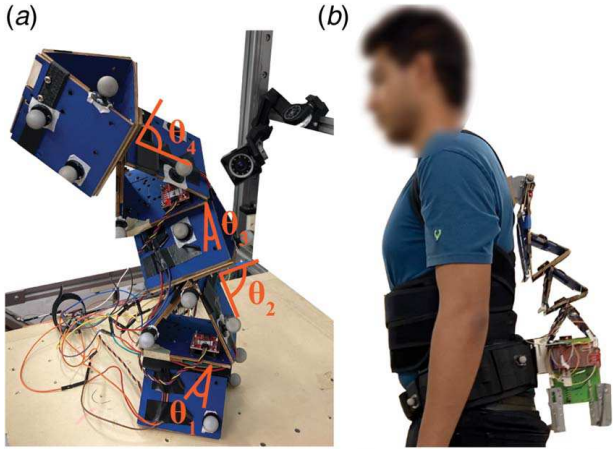

Fig. 1 Origami exoshell and experimental setup to evaluate the kinematic estimation of the fusion algorithm: (*a*) bench test setup and (*b*) test with the human user wearing the origami exoshell

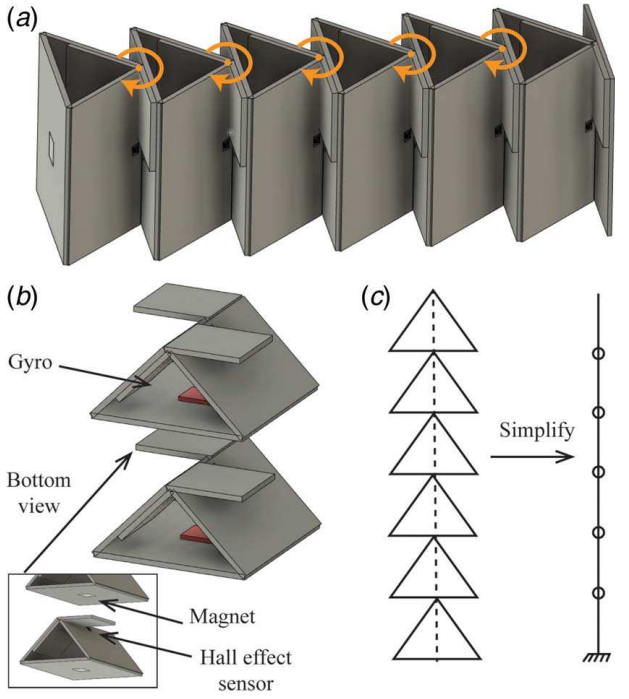

Fig. 2 (*a*) Origami exoshell design; arrows indicate the direction of rotation. (*b*) Hall effect sensors are mounted at each joint, and gyroscopes are mounted within each link. (c) The exoshell consists of triangular origami modules that when connected form a serial link robot with discrete joints.

study we aim at encoder- and magnetometer-free sensor configurations. We utilize Hall effect sensors and gyroscopes as these sensors are lightweight, compact, and do not affect the flexibility of the joints. This introduces additional challenges such as noisy measurements from the Hall sensor and drift due to gyroscope bias.

To mitigate the limitations of each individual sensor, we design a KF for sensor fusion of the gyroscopes and Hall effect sensors, to attenuate Hall effect sensor noise and compensate for drift due to gyroscope bias, which are the primary limitations of these sensors. The KF design is tailored toward our specific application: to estimate the human's torso and robot joint angles with a wearable serial link robot (with no fixed base frame). To compensate for drift, the bias related to the kinematics of each joint was included as a state estimate. Introducing these additional state estimates leads to the unobservability of the KF, specifically of the bias related to the torso kinematics. To handle this issue, we incorporate the forward kinematics of the robot into the KF as state constraints. Previous theoretical studies have noted the possibility of utilizing the state constraints to increase the observability of the KF [12], and through this work, we demonstrate this approach for improving estimation performance with a wearable serial link robot. The proposed algorithm was evaluated on the origami exoshell through bench tests and with human participants wearing the device. Our formulation is a general approach that can be applicable to many wearable robots that contain a kinematic chain, such as lower-limb exoskeletons [13–15], back spine robots [16–18], and many other devices similar to our origami exoshell.

The remainder of the paper is organized as follows. Section 2 discusses the exoshell robot design and sensor hardware, and Sec. 3 presents the formulation of our proposed algorithm: the Kinematically constrained Kalman filter (KCKF). Section 4 describes the experiments to evaluate the algorithm and presents the results along with a discussion. Finally, the conclusions and future work are discussed in Sec. 5.

2 System Hardware

The system consists of an origami exoshell robot with embedded sensors throughout the structure of the robot. The origami robot design and the sensors will be described in the following sections.

2.1 Origami Robot Design. The basic building module of the origami exoshell is a triangular origami link that enables one degree-of-freedom (DOF) rotational motion with a 60 deg range of motion (ROM). The triangular modules are connected next to each other to form a serial link robot, as depicted in Fig. 2. The modularity of this design allows the assembly of wearable serial link robots with multiple DOF that are capable of achieving rotational orientation in three dimensions (3D). The origami exoshell was designed to be worn on the back of the human, as shown in Fig. 1, in order to estimate and assist the user's torso motion. More details on the origami exoshell design can be found in Ref. [1].

The triangular modules are fabricated with two outer rigid layers of cardboard and a middle flexible polyester layer that forms a living hinge. The flexibility of the layer is the fundamental mechanism that allows 1DOF rotational motion of the origami. The selected materials are lightweight and have inherent compliance, ideal for wearable devices. As shown, the origami exoshell design avoids the use of heavy and rigid metal elements that could compromise the robot's lightweight and compliant characteristics. Rotary encoders are typically rigid and bulky metal devices. Therefore, embedding rotary encoders within the origami exoshell is not possible as it adds considerable weight and because there is limited area for mounting. Furthermore, the rigidness of typical encoders affects the robot's structural compliance, compromising the flexibility of the layer and therefore the mobility of the joint. As a solution, the origami robot was embedded with Hall effect sensors as an alternative to rotary encoders. Gyroscopes were also mounted at each module to obtain angular rate measurements of each link.

2.2 Hall Effect Sensors. Hall effect sensors (DRV5053, Texas Instrument, Dallas, TX) were used on the origami robot to measure the relative angle of the joint. These sensors do not compromise the exoshell design as they are compact and lightweight, with a size of 4 mm by 3 mm and a weight of 0.1 g. In contrast, a typical rotary encoder weighs approximately 100 g, demonstrating that a Hall effect sensor is more lightweight than an encoder by multiple orders of magnitude.

Hall effect sensors have the capability to sense the magnetic flux density. A pair of magnets and a Hall effect sensor were mounted on the joints of the origami robot, as depicted in Fig 2. In this scenario, changes in the joint angle lead to changes in the magnetic flux density measured by the Hall effect sensor, due to changes in alignment and proximity between the magnetic field and the sensor. As such, the Hall effect sensor exhibits a response to the joint angle state. This working principle allows using a Hall effect sensor for 1DOF joint angle estimation.

A sensor characterization was performed to analyze the sensor response to joint angle state. A cyclic motion was performed on a single origami hinge while recording Hall effect sensor measurements and ground truth measurements of the origami's joint angle obtained from a Motion Capture system (T40s, VICON Inc., Los Angeles, CA). The sensor response is presented in Fig. 3. An exponential curve fitting was performed over the Hall effect sensor characterization data to obtain a mathematical model that allows estimating the origami's joint angle. The model for one sensor is summarized in Eq. (1) in which V is the voltage measured from the sensor and θ_h is the estimated angle measurement of the Hall effect sensor.

$$\theta_h(V) = 0.07e^{2.87V} - (2.22 \times 10^5)e^{-8.43V} \tag{1}$$

The sensor characterization in Fig. 3 demonstrates a significant saturation for one side of the origami's joint angle (e.g., $\theta > 0$) which considerably affects the estimation performance for this region. As such, two Hall effect sensors were mounted on opposite sides of each joint in order to measure the complete ROM by operating simultaneously, as illustrated in Fig. 3.

2.3 Gyroscope Sensor. Gyroscope sensors (LSM6DSO, STMicroelectronics, Geneva, Switzerland) were used on the origami robot to measure the angular rate of the links and estimate the joint angular position. The gyroscopes were mounted on each link of the origami exoshell robot as demonstrated in Fig. 2. The relative orientation between each gyroscope was physically aligned to one another by means of design constraints and as such allowed the assumption that in the neutral position, the inertial frames of the gyroscopes are aligned. With this assumption, the angular rate of each joint can be computed by measuring the neighboring gyroscopes as follows:

$$\dot{\boldsymbol{\theta}}_{\boldsymbol{i}} = \boldsymbol{\omega}_{\boldsymbol{i}} - \boldsymbol{\omega}_{\boldsymbol{i-1}} \tag{2}$$

where $\dot{\boldsymbol{\theta}}_{\boldsymbol{i}} = \begin{bmatrix} \dot{\theta}_x & \dot{\theta}_y & \dot{\theta}_z \end{bmatrix}_i$ is the 3D angular speed of joint i with respect to the x-, y- and z-axes, and $\boldsymbol{\omega}_{\boldsymbol{i}} = \begin{bmatrix} \omega_x & \omega_y & \omega_z \end{bmatrix}_i$ is the gyroscope 3D angular rate measurement of link l_i with respect to the x-, y- and z-axes.

The joint angle can be estimated by integration of the joint's angular rate Eq. (2) obtained through the gyroscope measurements. However, a major disadvantage is that integration of the gyroscope signal leads to a drift in the joint angle estimate that decays performance over extended use.

3 Sensor Fusion With Kalman Filter

The origami robot was integrated with two different types of sensors: gyroscopes and Hall effect sensors. Both types of sensors have different sensing capabilities but complementary qualities for joint angle estimation. The Hall effect sensors are able to directly measure the joint angle state but provide a significantly noisier measurement. In contrast, gyroscopes provide a less noisy estimate of the joint angle but they suffer from bias which significantly affects the estimation performance over time. The limitations and advantages of each sensor have complementary properties to one another, as the Hall effect sensor can be used to compensate for the drift in the gyroscopes measurements, and the gyroscope provides a significantly less noisy measurement input. These complementary properties make sensor fusion an ideal method to overcome the individual limitations of each sensor and improve joint angle estimation performance.

3.1 Kalman Filter Algorithm Formulation. The KF was selected as the method to fuse the sensor information from the gyroscopes and the Hall effect sensors. The formulation of our KF will consider the general case of a serial link origami robot with n joints and 3DOFs at each joint. This formulation aims to estimate the 3D kinematics of the robot and the human.

The standard form of the KF for the discrete domain in state space system consists of the state transition Eq. (3) and the measurement Eq. (4)

$$\boldsymbol{x}(k+1) = A\boldsymbol{x}(k) + B\boldsymbol{u}(k) + \boldsymbol{\nu}(k) \tag{3}$$

$$\boldsymbol{y}(k) = C\boldsymbol{x}(k) + \boldsymbol{v}(k) \tag{4}$$

where $\boldsymbol{x}(k) \in \mathbb{R}^{(6n+6)\times 1}$ and $\boldsymbol{y}(k) \in \mathbb{R}^{(6n+3)\times 1}$ are the system state and measurement vector at time k; $\boldsymbol{\nu}(k)$, and $\boldsymbol{v}(k)$ are the process noise and measurement noise with covariances $Q \in \mathbb{R}^{(6n+6)\times(6n+6)}$ and $R \in \mathbb{R}^{(6n+3)\times(6n+3)}$.

Considering a serial link robot with n joints, and two Hall effect sensors per joint, the system measurement is given by (5)

$$\boldsymbol{y}(k) = \begin{bmatrix} \boldsymbol{\theta}^{\boldsymbol{l}}_{\boldsymbol{h_1}}(k) & \boldsymbol{\theta}^{\boldsymbol{r}}_{\boldsymbol{h_1}}(k) & \cdots & \boldsymbol{\theta}^{\boldsymbol{l}}_{\boldsymbol{h_n}}(k) & \boldsymbol{\theta}^{\boldsymbol{r}}_{\boldsymbol{h_n}}(k) \end{bmatrix}^T \tag{5}$$

where $\boldsymbol{\theta}^{\boldsymbol{l}}_{\boldsymbol{h_i}} = \begin{bmatrix} \theta^l_{hx} & \theta^l_{hy} & \theta^l_{hz} \end{bmatrix}_i$ and $\boldsymbol{\theta}^{\boldsymbol{r}}_{\boldsymbol{h_i}} = \begin{bmatrix} \theta^r_{hx} & \theta^r_{hy} & \theta^r_{hz} \end{bmatrix}_i$ are the left side ($\boldsymbol{\theta}^{\boldsymbol{l}}_{\boldsymbol{h_i}}$) and right side ($\boldsymbol{\theta}^{\boldsymbol{r}}_{\boldsymbol{h_i}}$) Hall effect sensor angle measurements of joint i with respect to the x-, y-, and z-axes.

The input to the system is the angular rate, as it is imposed by the human's movement.

$$\boldsymbol{u}(k) = \begin{bmatrix} \boldsymbol{\omega_1}(k) & \boldsymbol{\omega_2}(k) & \cdots & \boldsymbol{\omega_{n+1}}(k) \end{bmatrix}^T \tag{6}$$

The system states $\boldsymbol{x}(k)$ include the robot joint angles $\boldsymbol{\theta_i} = \begin{bmatrix} \theta_x & \theta_y & \theta_z \end{bmatrix}_i$ and the human torso angles $\boldsymbol{\phi_i} = \begin{bmatrix} \phi_x & \phi_y & \phi_z \end{bmatrix}_i$ with respect to the x-, y- and z-axes, as depicted in Fig. 4. The human torso angle $\boldsymbol{\phi}$ corresponds to the robot's end-effector orientation with respect to the base frame, as shown in Fig. 4(*b*). To compensate for gyroscope drift, the system state of the standard KF was augmented to include an estimation of the gyroscope sensor bias $\boldsymbol{b_i}$. The system states are given by Eq. (7), where $\boldsymbol{b_i} = \begin{bmatrix} b_x & b_y & b_z \end{bmatrix}_i$ are the gyroscope bias corresponding to joint i,

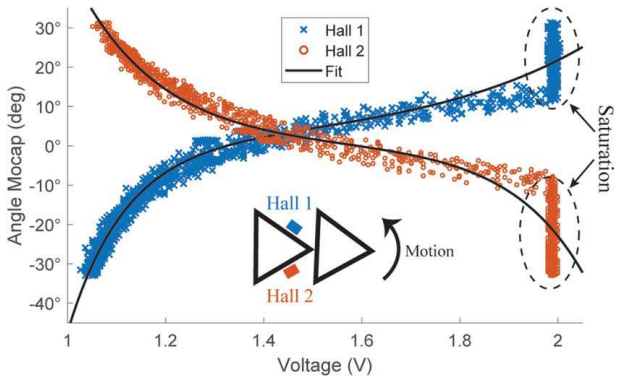

Fig. 3 Hall effect sensors characterization plot. Two Hall effect sensors are placed on opposite sides of the origami joint, depicted as colored boxes in the illustration.

and $\boldsymbol{b_\phi} = \begin{bmatrix} b_x & b_y & b_z \end{bmatrix}_\phi$ is the bias corresponding to $\boldsymbol{\phi}$.

$$\boldsymbol{x}(k) = [\,\boldsymbol{\theta_1}(k)\ \boldsymbol{\theta_2}(k)\ \cdots\ \boldsymbol{\theta_n}(k)\ \boldsymbol{\phi}(k)\ \boldsymbol{b_1}(k)\ \boldsymbol{b_2}(k)\ \cdots\ \boldsymbol{b_n}(k)\ \boldsymbol{b_\phi}(k)\,]^T \tag{7}$$

With this formulation, the measurement matrix C is

$$C = \begin{bmatrix} I_3 & 0_3 & \cdots & 0_3 & 0_3 & \cdots & 0_3 \\ I_3 & 0_3 & \cdots & 0_3 & 0_3 & \cdots & 0_3 \\ 0_3 & I_3 & \cdots & 0_3 & 0_3 & \cdots & 0_3 \\ 0_3 & I_3 & \cdots & 0_3 & 0_3 & \cdots & 0_3 \\ \vdots & \vdots & \ddots & \vdots & \vdots & \ddots & \vdots \\ 0_3 & 0_3 & \cdots & I_3 & 0_3 & \cdots & 0_3 \\ 0_3 & 0_3 & \cdots & I_3 & 0_3 & \cdots & 0_3 \end{bmatrix} \tag{8}$$

where I_n is an $n \times n$ identity matrix, and 0_n represents a $n \times n$ matrix with all elements being zero. The structure of the measurement matrix C shows that for each joint two Hall effect sensors measure simultaneously the angle state to avoid loss of information due to sensor saturation.

For the process model of the system, we assume the following discrete first-order dynamic model

$$\boldsymbol{\theta_i}(k+1) = \boldsymbol{\theta_i}(k) + (\boldsymbol{\omega_{i+1}}(k) - \boldsymbol{\omega_i}(k) - \boldsymbol{b_i}(k))t_s \tag{9}$$

where t_s is the time between sampled measurements. The process model in Eq. (9) describes the evolution of the joint angle state and incorporates the gyroscope measurement and its related drift due to sensor bias.

Similarly, the process model for the human's torso angle is given by Eq. (10). The human torso angle $\boldsymbol{\phi}$ corresponds to the robot's end-effector orientation with respect to the base, as depicted in Fig. 4, and therefore utilizes the gyroscope measurements of the base ($\boldsymbol{\omega_1}$) and the end-effector link ($\boldsymbol{\omega_{n+1}}$) to simulate a virtual joint. To compensate for the combined bias effect of the two gyroscopes at the distal ends of the robot, a bias of the virtual joint $\boldsymbol{b_\phi}$ is incorporated into the process model

$$\boldsymbol{\phi}(k+1) = \boldsymbol{\phi_i}(k) + (\boldsymbol{\omega_{n+1}}(k) - \boldsymbol{\omega_1}(k) - \boldsymbol{b_\phi}(k))t_s \tag{10}$$

According to this process model, the transition matrix A is given by Eq. (11)

$$A = \begin{bmatrix} I_3 & 0_3 & \cdots & 0_3 & 0_3 & -I_3t_s & 0_3 & \cdots & 0_3 & 0_3 \\ 0_3 & I_3 & \cdots & 0_3 & 0_3 & 0_3 & -I_3t_s & \cdots & 0_3 & 0_3 \\ \vdots & \vdots & \ddots & \vdots & \vdots & \vdots & \vdots & \ddots & \vdots & \vdots \\ 0_3 & 0_3 & \cdots & I_3 & 0_3 & 0_3 & 0_3 & \cdots & -I_3t_s & 0_3 \\ 0_3 & 0_3 & \cdots & 0_3 & I_3 & 0_3 & 0_3 & \cdots & 0_3 & -I_3t_s \\ 0_3 & 0_3 & \cdots & 0_3 & 0_3 & I_3 & 0_3 & \cdots & 0_3 & 0_3 \\ 0_3 & 0_3 & \cdots & 0_3 & 0_3 & 0_3 & I_3 & \cdots & 0_3 & 0_3 \\ \vdots & \vdots & \ddots & \vdots & \vdots & \vdots & \vdots & \ddots & \vdots & \vdots \\ 0_3 & 0_3 & \cdots & 0_3 & 0_3 & 0_3 & 0_3 & \cdots & I_3 & 0_3 \\ 0_3 & 0_3 & \cdots & 0_3 & 0_3 & 0_3 & 0_3 & \cdots & 0_3 & I_3 \end{bmatrix} \tag{11}$$

The input model is given by the matrix in Eq. (12) according to the process model

$$B = \begin{bmatrix} -I_3t_s & I_3t_s & 0_3 & \cdots & 0_3 & 0_3 \\ 0_3 & -I_3t_s & I_3t_s & \cdots & 0_3 & 0_3 \\ 0_3 & 0_3 & -I_3t_s & \cdots & 0_3 & 0_3 \\ \vdots & \vdots & \vdots & \ddots & \vdots & \vdots \\ 0_3 & 0_3 & 0_3 & \cdots & -I_3t_s & I_3t_s \\ -I_3t_s & 0_3 & 0_3 & \cdots & 0_3 & -I_3t_s \\ & & 0_{3n+3} & & & \end{bmatrix} \tag{12}$$

Then, the process noise covariance for this model is

$$Q = \begin{bmatrix} \frac{t_s^4}{4} I_{(3n+3)} & \frac{t_s^3}{2} I_{(3n+3)} \\ \frac{t_s^3}{2} I_{(3n+3)} & t_s^2 I_{(3n+3)} \end{bmatrix} \tag{13}$$

In Sec. 3.2, the standard formulation of the KF will be augmented to incorporate state constraints over the joint kinematics.

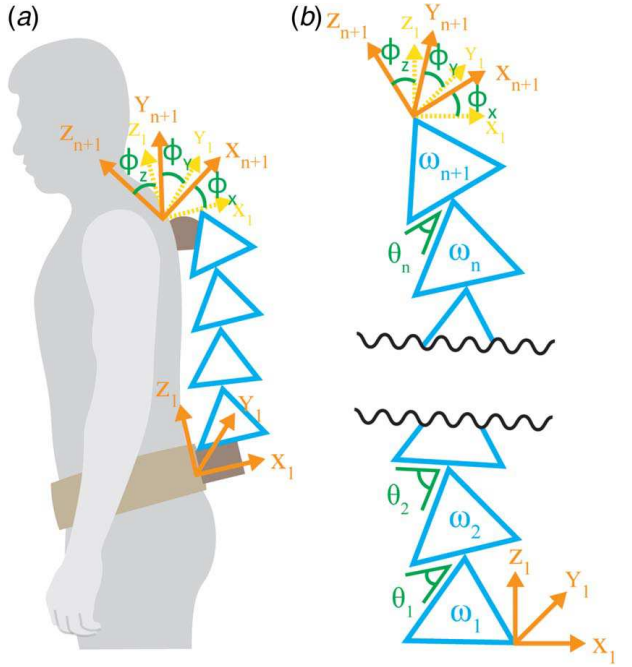

Fig. 4 (*a*) Human wearing the origami exoshell robot; torso angles ϕ correspond to the relative orientation between the coordinate frames of the top and bottom body segments. (*b*) Illustration of the origami exoshell robot with state variables; the torso angles ϕ correspond to the relative orientation between the coordinate frames of the base and the end-effector links of the origami robot.

3.2 State Constraints in the Kalman Filter. Since the origami robot consists of a series of interconnected links, there exists a kinematic chain that imposes state dependencies between a particular joint and the subsequent joints. Examining the illustration in Fig. 4, we can identify that the human torso angle corresponds to the end-effector orientation, which can also be obtained through the forward kinematics of the robot. For a serial link robot, the equation of the forward kinematics F depends on the states of all the robot joints. In our case, the forward kinematics that relates to the human torso angle are given by Eq. (14)

$$\boldsymbol{\phi} = F(\boldsymbol{\theta}) = \Sigma\boldsymbol{\theta_i} = \boldsymbol{\theta_1} + \boldsymbol{\theta_2} + \cdots + \boldsymbol{\theta_n} \tag{14}$$

The forward kinematics equation provides an equality state constraint in the form of Eq. (15), which can be implemented into the KF

$$D\boldsymbol{x}(k) = \boldsymbol{d} \tag{15}$$

The KF measurement equation can be augmented to include equality state constraints by treating it as a perfect measurement as shown in Eq. (16), where $\mathbf{0_{3,1}}$ represents a 3×1 vector with all elements being zero

$$\begin{bmatrix} \boldsymbol{y}(k) \\ \boldsymbol{d} \end{bmatrix} = \begin{bmatrix} C \\ D \end{bmatrix} \boldsymbol{x}(k) + \begin{bmatrix} \boldsymbol{v}(k) \\ \mathbf{0_{3,1}} \end{bmatrix} \tag{16}$$

In this context, the corresponding values for the variables of the state constraints are $\boldsymbol{d} = \begin{bmatrix} 0 & 0 & 0 \end{bmatrix}^T$, and

$$D = \begin{bmatrix} I_3 & I_3 & \cdots & I_3 & -I_3 & 0_3 & 0_3 & 0_3 & \cdots & 0_3 & 0_3 \end{bmatrix} \quad (17)$$

To incorporate the kinematic state constraints into the KF formulation, the measurement vector and the measurement matrix were augmented as shown below

$$\boldsymbol{y}(k)_{KCKF} = \begin{bmatrix} \boldsymbol{\theta}^l_{\boldsymbol{h}_1}(k) & \boldsymbol{\theta}^r_{\boldsymbol{h}_1}(k) & \cdots & \boldsymbol{\theta}^l_{\boldsymbol{h}_n}(k) & \boldsymbol{\theta}^r_{\boldsymbol{h}_n}(k) & \mathbf{0}_{1,3} \end{bmatrix}^T \quad (18)$$

$$C_{KCKF} = \begin{bmatrix} I_3 & 0_3 & \cdots & 0_3 & 0_3 & 0_3 & 0_3 & \cdots & 0_3 & 0_3 \\ I_3 & 0_3 & \cdots & 0_3 & 0_3 & 0_3 & 0_3 & \cdots & 0_3 & 0_3 \\ 0_3 & I_3 & \cdots & 0_3 & 0_3 & 0_3 & 0_3 & \cdots & 0_3 & 0_3 \\ 0_3 & I_3 & \cdots & 0_3 & 0_3 & 0_3 & 0_3 & \cdots & 0_3 & 0_3 \\ \vdots & \vdots & \ddots & \vdots & \vdots & \vdots & \vdots & \ddots & \vdots & \vdots \\ 0_3 & 0_3 & \cdots & I_3 & 0_3 & 0_3 & 0_3 & \cdots & 0_3 & 0_3 \\ 0_3 & 0_3 & \cdots & I_3 & 0_3 & 0_3 & 0_3 & \cdots & 0_3 & 0_3 \\ I_3 & I_3 & \cdots & I_3 & -I_3 & 0_3 & 0_3 & \cdots & 0_3 & 0_3 \end{bmatrix} \quad (19)$$

Now, according to the modified measurement equation, the measurement noise covariance R is given by

$$R = \begin{bmatrix} \sigma^2_{hall} I_{6n} & 0_{6n\times 3} \\ 0_{3\times(6n+3)} \end{bmatrix} \quad (20)$$

where $0_{n\times m}$ represents an $n \times m$ matrix with all elements being zero, and σ_{hall} is the standard deviation of the Hall effect sensor noise which was obtained experimentally ($\sigma_{hall} = 3.2$ deg).

3.3 Observability of the Kalman Filter. A KF with a system of unobservable states will not converge to a meaningful solution, since by definition, an unobservable state is one in which no information may be obtained through the measurement equations [19]. The observability of the KCKF was analyzed, which takes into account the process model (3) and measurement Eq. (4). A system with a state vector $\boldsymbol{x}(k)$ of dimension N is observable if the observability matrix O defined in Eq. (21) has a row rank N

$$O = \begin{bmatrix} C \\ CA \\ \vdots \\ CA^i \\ \vdots \\ CA^{N-1} \end{bmatrix} \quad (21)$$

We computed the observability matrix O and analyzed the observability of each state variable by inspecting that the corresponding column vector of O is linearly independent. The observability matrix of the KCKF, defined by Eqs. (11) and (19), has row rank N, which implies that the system has full observability of all the states. In contrast, the observability matrix of the standard KF, defined by Eqs. (11) and (8), which does not incorporate the kinematic state constraints, has a row rank $N - 6$, which reveals that the system is unobservable. Specifically, the state variables that are unobservable are the 3D torso angle $\boldsymbol{\phi}$ and its related bias $\boldsymbol{b}_{\boldsymbol{\phi}}$.

The observability analysis reveals that incorporating forward kinematics as state constraints contributes to achieving the observability of the system. This is because the KCKF treats the forward kinematics of the robot as measurements and provides information on the torso angle state $\boldsymbol{\phi}$ in Eq. (10), which combined with Eq. (9) permits observability of the related bias state $\boldsymbol{b}_{\boldsymbol{\phi}}$.

4 Experiments, Results and Discussion of Fusion Algorithm Performance

The estimation performance of the sensor fusion algorithm was verified with the origami exoshell design presented in Fig. 1. The joint kinematics of the origami robot was estimated with the sensor fusion algorithm and compared to ground truth measurements obtained from a motion capture system. Three types of experiments were performed to evaluate the performance of the algorithm: cyclic motion test, extended use test, and evaluation with a human user. Through the experiments, we will demonstrate the capability of our fusion algorithm to (1) attenuate sensor noise, (2) compensate drift due to sensor bias, (3) be robust for extended use, and (4) be capable of improving kinematic estimation performance.

4.1 Cyclic Motion Experiments. The motion performed on the origami robot was aimed to mimic the human's motion during gait. A cyclic motion, similar to the motion of the human's torso during walking, was manually induced on the origami robot.

The experimental setup can be seen in Fig. 1(*a*). For this experiment, the origami robot consisted of five links and four joints ($n = 4$). Two of the joints allowed rotation about the x-axis (θ_1 and θ_3) and the other two about the y-axis (θ_2 and θ_4). With this configuration, the origami robot can perform rotational motion in two dimensions (2D). Therefore, the KCKF will estimate the robot's and the human's 2D joint kinematics.

4.1.1 Results of Sensor Fusion and Individual Sensors. The results of the sensor fusion estimation and the individual's sensor estimation through the experiment for two robot joints (θ_{3x} and θ_{4y}) are presented in Fig. 5. This figure compares the kinematics estimation obtained from each individual sensor and the estimation from the proposed KCKF. In this figure, it can be observed that the Hall effect sensor produces noisy estimates that deviate from the true value, especially at high joint angles. In addition, the angle estimation obtained from the gyroscope integration demonstrates significant drift, which can be easily visualized at the end of the experiment, approximately after 90 s. The proposed KCKF sensor fusion algorithm provided a smooth and drift-free joint angle estimate, compared to Hall sensor measurements and gyroscope integration, respectively.

The root-mean-square errors (RMSE) for the complete trial were computed using the motion capture data as ground truth. The joint angle RMSE of the individual sensors and the fusion algorithm are

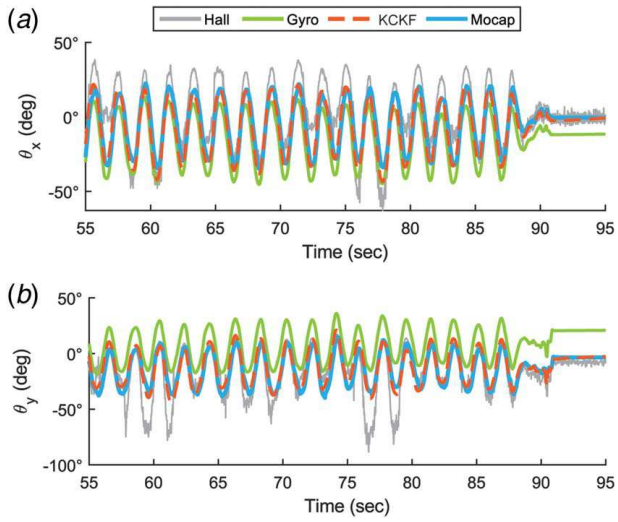

Fig. 5 Joint kinematic estimation of individual sensors and the KCKF sensor fusion algorithm. Included are the robot kinematics of (*a*) θ_3 (*x*-axis rotation), and (*b*) θ_4 (*y*-axis rotation).

Table 1 RMSE (deg) of kinematic estimation

Joint	Gyro	Hall 1	Hall 2	Std KF	KCKF
θ_{1x}	31.66	20.96	14.33	5.29	5.07
θ_{2y}	9.78	14.74	10.06	6.12	6.11
θ_{3x}	3.70	6.62	6.04	3.41	3.46
θ_{4y}	20.25	12.13	7.44	6.11	6.00
ϕ_x	11.41	–	–	50.27	5.14
ϕ_y	44.01	–	–	17.98	5.94

summarized in Table 1. The overall results reveal that the sensor fusion algorithm is capable of significantly reducing the RMSE compared to the estimates obtained from individual sensors. Our proposed fusion algorithm achieves a maximum RMSE reduction of approximately 87% compared to the estimate of the lowest performing sensor. Furthermore, the fusion algorithm was consistent in improving the kinematic estimate for each joint of the complete robot with overall better performance than the baseline sensor estimation.

The results of this experiment demonstrated that the proposed KCKF has the capability to overcome individual sensor limitations, as the fusion estimate attenuated noise-related error from the Hall sensor and compensated drift due to gyroscope sensor bias. Compared to the estimation from each individual sensor, our proposed algorithm provides a joint angle estimate that is closer to ground truth.

4.1.2 Results of Kinematic State Constraints in Kalman Filter. The results of the torso kinematic estimation from the fusion algorithm and the motion capture are presented in Fig. 6. This figure includes a comparison of the KCKF and the standard KF without state constraints. The RMSE for the KCKF and the standard KF are summarized in Table 1. The results reveal that incorporating state constraints improves the overall estimation performance compared to the standard KF, with a maximum RMSE reduction of approximately 90% for the torso angle (ϕ) estimation. The difference in performance is due to the fact that the state constraints contribute to having full observability of the system and enable estimating the state of the torso angle and its related bias, as discussed in Sec. 3.3. Without the state constraints, it is challenging to achieve acceptable performance with the standard KF as it is unable to compensate for the sensor bias that leads to drift. This result demonstrates the implications of incorporating the robot's forward kinematics into the KF as state constraints on the estimation performance of unobservable states.

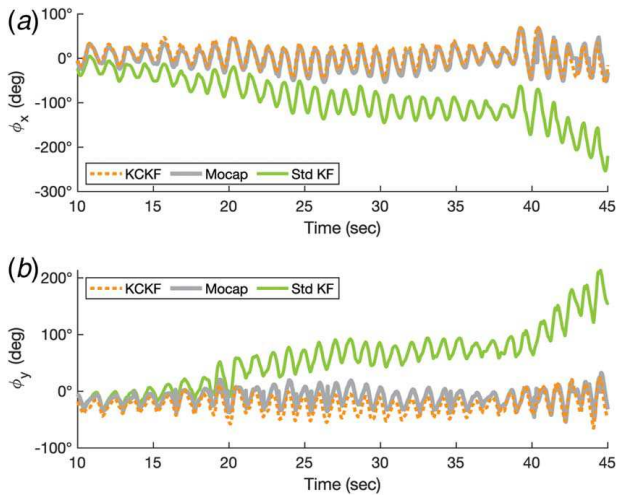

Fig. 6 Comparison of the KCKF and the standard KF. The results include the torso angle: (*a*) in the sagittal plane (*x*-axis) and (*b*) in the lateral plane (*y*-axis).

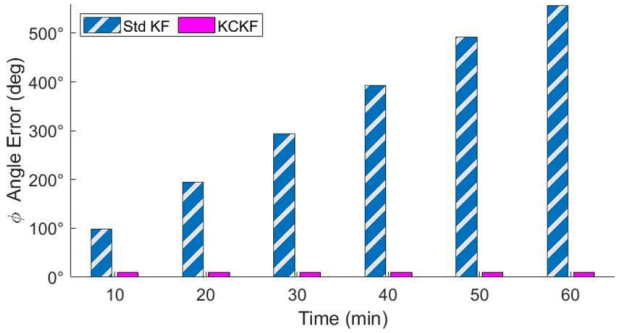

Fig. 7 Drift of kinematic estimation over 1 h

4.2 Extended Use Test. As a wearable device, one requirement for the algorithm is that it is robust through the use of a complete day. Long-duration tests were performed to verify that the algorithm's performance does not decay significantly through extended use. The test protocol consisted of introducing an initial movement on the origami robot and then fixing the position for an extended period of time to analyze the drift. To verify extended performance, the KCKF was tested on the origami robot for a duration of 1 h and the drift was compared with the standard KF. The drift of the kinematic estimate for one joint throughout the experiment is plotted in Fig. 7. Over the extension of 1 h, it is visible that the proposed KCKF is capable of accurately estimating joint kinematics and compensates for the significant drift that the gyroscope bias induces. By the end of the 1-h trial, the standard KF had drifted by approximately 550 deg, while our proposed KCKF algorithm was still within 7 deg of the true value. The results demonstrate that the KCKF maintains estimation performance through extended use and that our proposed formulation exceeds the standard KF performance.

4.3 Testing with Human Subject. The performance of the KCKF was evaluated with a human user for estimating the torso kinematics while performing activities of daily living. One healthy participant (28 years, 86 kg, 1.7 m) was recruited for this study. The experimental setup with the human user wearing the origami robot can be seen in Fig. 1(*b*). In this experiment, the subject performed a bending and extension motion (with 30 deg ROM) of the upper torso that mimics the cyclic movement in activities such as walking or repetitive lifting.

The human torso kinematics estimated by the KCKF is presented in Fig. 8. The results reveal that when the exoshell is worn, the

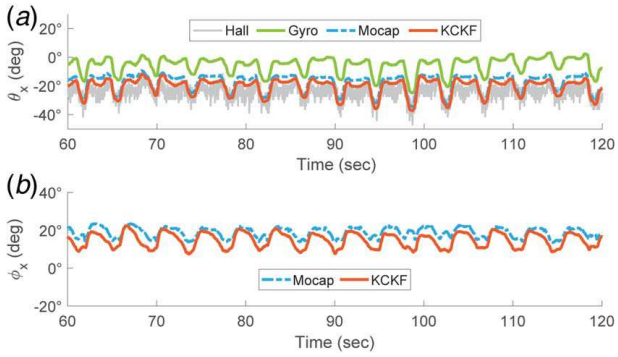

Fig. 8 Kinematic estimation while wearing the origami exoshell robot. The plots include (*a*) the robot kinematics for θ_2 and (*b*) the human's torso kinematics ϕ.

KCKF can accurately estimate the torso joint angle, with 4.85-deg RMSE. Figure 8(*b*) shows that the kinematic estimation captures the cyclic profile of the torso's movement, which is required for the control of the origami robot. This experiment revealed the existence of interaction forces between the robot and the user that cause sensor misalignment. We observed that sensor placement shifted when there was compression and over-extension of the robot. Compression occurred when the torso was straight (i.e., when $\boldsymbol{\phi}$ is close to 0 deg) and over-extension when the torso was bending (i.e., when $\boldsymbol{\phi}$ reaches its maximum), both of which cause estimation error during those instances, as seen in Fig. 8(*b*).

5 Conclusions

In this work, we presented the formulation of the KCKF, a sensor fusion algorithm tailored for a wearable origami serial link robot. Our unique origami exoshell design has inherent constraints that require an encoder- and magnetometer-free sensor configuration. We developed a sensor fusion algorithm that uses gyroscopes and Hall effect sensors, as they are compatible sensors, but are affected by noise and sensor bias. Building upon the early theory in KF, this work demonstrates through experiments the benefits of incorporating the robot's forward kinematics as state constraints in order to address the unobservability of the system. The results demonstrate that our proposed KCKF improves state estimation performance, compared to the individual sensor measurements and the standard KF. Future work includes implementing the KCKF for real-time control of the origami exoshell robot. We plan to expand the formulation of our KCKF algorithm to incorporate dynamics of the exoshell to estimate interaction forces between the robot and the user for more precise control of the robot.

Acknowledgment

The authors gratefully acknowledge the financial support from "The Global KAITEKI Center" at Arizona State University (ASU), a university–industry partnership between ASU and The KAITEKI Institute of Mitsubishi Chemical Group Corporation.

Conflict of Interest

There are no conflicts of interest.

Data Availability Statement

The data sets generated and supporting the findings of this article are obtainable from the corresponding author upon reasonable request.

References

[1] Li, D., Yumbla, E. Q., Olivas, A., Sugar, T., Amor, H. B., Lee, H., Zhang, W., and Aukes, D. M., 2022, "Origami-Inspired Wearable Robot for Trunk Support," IEEE/ASME Trans. Mechatron., pp. 1–11.

[2] Yumbla, E. Q., Qiao, Z., Tao, W., and Zhang, W., 2021, "Human Assistance and Augmentation With Wearable Soft Robotics: A Literature Review and Perspectives," Curr. Robot. Rep., **2**(12), pp. 399–413.

[3] Tiboni, M., Borboni, A., Vérité, F., Bregoli, C., and Amici, C., 2022, "Sensors and Actuation Technologies in Exoskeletons: A Review," Sensors, **22**(3), p. 884.

[4] Yumbla, F., Yumbla, W., Yumbla, E. Q., and Moon, H., 2022, "Oobsoft Gripper: A Reconfigurable Soft Gripper Using Oobleck for Versatile and Delicate Grasping," Proceedings of the 2022 IEEE 5th International Conference on Soft Robotics (RoboSoft), Edinburgh, UK, Apr. 4–8, pp. 512–517.

[5] Filippeschi, A., Schmitz, N., Miezal, M., Bleser, G., Ruffaldi, E., and Stricker, D., 2017, "Survey of Motion Tracking Methods Based on Inertial Sensors: A Focus on Upper Limb Human Motion," Sensors, **17**(6), p. 1257.

[6] Wittmann, F., Lambercy, O., and Gassert, R., 2019, "Magnetometer-Based Drift Correction During Rest in Imu Arm Motion Tracking," Sensors, **19**(6), p. 1312.

[7] Ahmad, N., Ghazilla, R. A. R., Khairi, N. M., and Kasi, V., 2013, "Reviews on Various Inertial Measurement Unit (IMU) Sensor Applications," Int. J. Signal Process. Syst., **1**(2), pp. 256–262.

[8] Lee, J. K., and Choi, M. J., 2019, "Robust Inertial Measurement Unit-Based Attitude Determination Kalman Filter for Kinematically Constrained Links," Sensors, **19**(4), p. 768.

[9] Jeon, S., Tomizuka, M., and Katou, T., 2009, "Kinematic Kalman Filter (KKF) for Robot end-Effector Sensing," ASME J. Dyn. Syst. Meas. Control., **131**(2), p. 021010.

[10] Xu, C., He, J., Zhang, X., Yao, C., and Tseng, P.-H., 2018, "Geometrical Kinematic Modeling on Human Motion Using Method of Multi-Sensor Fusion," Inf. Fusion, **41**(1), pp. 243–254.

[11] Ponraj, G., and Ren, H., 2018, "Sensor Fusion of Leap Motion Controller and Flex Sensors Using Kalman Filter for Human Finger Tracking," IEEE Sens. J., **18**(3), pp. 2042–2049.

[12] Alouani, A., Blair, W., and Watson, G., 1991, "Bias and Observability Analysis of Target Tracking Filters Using a Kinematic Constraint," Proceedings of the Twenty-Third Southeastern Symposium on System Theory, Columbia, SC, Mar. 10–12, IEEE Computer Society Press, pp. 229–232.

[13] Esquenazi, A., Talaty, M., Packel, A., and Saulino, M., 2012, "The Rewalk Powered Exoskeleton to Restore Ambulatory Function to Individuals With Thoracic-Level Motor-Complete Spinal Cord Injury," Am. J. Phys. Med. Rehabil., **91**(11), pp. 911–921.

[14] Zoss, A., Kazerooni, H., and Chu, A., 2006, "Biomechanical Design of the Berkeley Lower Extremity Exoskeleton (Bleex)," IEEE/ASME Trans. Mechatron., **11**(4), pp. 128–138.

[15] Tsukahara, A., Kawanishi, R., Hasegawa, Y., and Sankai, Y., 2010, "Sit-to-Stand and Stand-to-Sit Transfer Support for Complete Paraplegic Patients With Robot Suit HAL," Adv. Rob., **24**(1), pp. 1615–1638.

[16] Yang, X., Huang, T.-H., Hu, H., Yu, S., Zhang, S., Zhou, X., Carriero, A., Yue, G., and Su, H., 2019, "Spine- Inspired Continuum Soft Exoskeleton for Stoop Lifting Assistance," IEEE Robot. Autom. Lett., **4**(10), pp. 4547–4554.

[17] Song, J., Zhu, A., Tu, Y., and Zou, J., 2021, "Multijoint Passive Elastic Spine Exoskeleton for Stoop Lifting Assistance," Int. J. Adv. Rob. Syst., **18**(6), p. 172988142110620.

[18] Roveda, L., Savani, L., Arlati, S., Dinon, T., Legnani, G., and Molinari Tosatti, L., 2020, "Design Methodology of an Active Back-Support Exoskeleton with Adaptable Backbone-Based Kinematics," Int. J. Ind. Ergon., **79**(1), p. 102991.

[19] Southall, B., Buxton, B. F., and Marchant, J. A., 1998, "Controllability and Observability: Tools for Kalman Filter Design," British Machine Vision Conference, Southampton, UK, Sept. 14–17, BMVA Press, pp. 17.1–17.10.